Dual-polarized printed cylindrical metasurface cloak at microwave frequencies

Hakjune Lee and Do-Hoon Kwon[*]

*Department of Electrical and Computer Engineering, University of Massachusetts Amherst, Amherst,
Massachusetts 01003, USA*

A printed metasurface on a grounded, thin cylindrical-shell dielectric substrate is introduced, capable of concealing large objects under both transverse electric and magnetic polarizations. When a plane wave illuminates the cylinder, the metasurface effectively absorbs the incident power on the lit side by inducing surface waves, and transports it to the shadow side before reconstructing the incident wavefront and thereby achieving cloaking. For each polarization, the surface waves are built and meticulously optimized to meet local and global lossless and gainless conditions, ensuring a passive surface characterization. Retrieved from the optimized complete tangential fields, a spatially modulated tensor surface reactance is realized using an array of printed Jerusalem-cross-shaped conductor patterns. At a microwave frequency, a prototype cloak is designed, fabricated, and experimentally characterized for its scattering properties. Measurement results confirm the effectiveness of the cloaking approach and its printed metasurface realization.

I. INTRODUCTION

The quest for effective cloaking has captivated the scientific community, with a goal of developing materials and technologies capable of rendering objects invisible in acoustic, microwave, and optical regimes. Cloaking technology has a wide range of potential applications of modern significance, such as stealth technology for the military, noninvasive sensing with an enhanced resolution, and interference mitigation in wireless communication systems. The principle of cloaking lies in manipulating the path of waves so that they flow around an object, leaving it undetectable using external sensors. To that end, several promising approaches have been introduced and developed in recent years.

The concept of transformation optics (TO) is based on the form invariance of Maxwell's equations, and a TO-based cloak coordinates the direction of incident waves to detour around the hidden region without reflections and scattering [1,2]. Metamaterials, three-dimensional volumetric structures of which the permittivity ϵ and the permeability μ are engineered, can realize effective media featuring unusual properties such as negative ϵ and/or μ, and a zero index of refraction, which are not found in nature. In particular, for TO-based cloaking, metamaterial shells consisting of spatially varying anisotropic unit cells have been proposed and experimentally demonstrated for cloaking cylindrical- [3] and rhombus-shaped [4] objects.

To alleviate the realization challenge associated with the anisotropy of cloak parameters, a spherical invisibility cloak design comprising isotropic multilayer shells has been reported [5]. The TO approach can be applied to carpet cloaking, which hides an object inside a bump on a ground plane [6]. The main advantages of the TO approach are that cloaking is achieved for any incident wave and a large object can be theoretically concealed. However, experimental TO cloaks have a metamaterial shell that is as thick as or thicker than the cloaked region. To realize a thin TO cloak, metamaterials with ϵ and μ of extreme values and high spatial anisotropy are needed, which are difficult to achieve in practice. Furthermore, the structural complexity of the metamaterial cells makes the physical construction of volumetric cloaks challenging.

Mantle and plasmonic cloaking reduces scattering of an object by canceling the dominant terms in the spatial harmonic expansion of the scattered field. Introduced in 2009 [7], it is the first cloaking scheme enabled by a surface structure. A thin homogeneous shell encloses the target object to be cloaked, represented by a position-independent design parameter—a relative permittivity ϵ_r for the plasmonic cloaking shell and a surface impedance Z_s for the mantle cloaking screen. A dielectric cylinder is enclosed by an array of metallic fins embedded in a high permittivity material, reducing the total scattering width [8]. The surface impedance Z_s is physically designed with a frequency-selective surface (FSS) composed of conductor patterns in various shapes [9–11], effectively mitigating scatterings from dielectric and/or conducting

---

[*]Corresponding author: dhkwon@umass.edu

cylinders at a desired frequency. Multiple-layer cloak shells are used to increase the size of the object or to extend the bandwidth [12]. Active elements are integrated into FSS-type structures to enhance existing passive cloaks [13], which can expand the bandwidth [14] and enable reconfigurability [13,15]. At terahertz frequencies, a reconfigurable mantle cloak is achieved by employing a single-atom layer of graphene with a tunable conductivity [16]. Not limited to electromagnetic applications, the mantle cloak approach has been extended to the acoustic regime, suppressing diffractions of acoustic waves by soft and hard cylinders [17]. While the scattering cancellation method effectively reduces scattering in the quasistatic regime, it has limitations for electrically large objects because the phase of the incident wave varies significantly across the scatterer volume.

Active cloaking employing an array of radiating sources that surround a target object has been introduced [18–20], and experimentally demonstrated with loop [21] and dipole [22] array antennas surrounding a perfect electric conductor (PEC) cylinder. The primary challenges in active cloaking include accurately sensing the incident wave, managing mutual interference, and mitigating potential instabilities in amplifiers.

As a two-dimensional (2D) variant of volumetric metamaterials, metasurfaces can control and manipulate fields at a reduced loss using a single layer of resonant inclusions [23]. Therefore, they can be utilized in invisibility cloak designs. A gradient metasurface on a zero-index material (ZIM) surrounding a to-be-cloaked region can enable full acceptance of the incident wave into the ZIM on the lit side, and release transmitted waves from the ZIM on the shadow side with the wavefronts aligned with the incident wave, thereby achieving invisibility [24]. Based on the generalized sheet transition conditions, a penetrable Omega-bianisotropic metasurface (O-BMS) cloak for an arbitrary shaped object was presented [25], characterized by spatially varying the scalar electric impedance Z_{se}, magnetic admittance Y_{sm}, and magnetoelectric coupling K_{em}. Recently, concentric multilayer BMSs have been designed for omnidirectional and nonreciprocal cloaking [26].

Metasurfaces are capable of not only manipulating wave reflection and transmission properties, but are also adept at converting the type of wave, such as transforming a plane wave (PW) into a surface wave (SW), and vice versa [27–29]. Using this capability, a printed metasurface for cylindrical cloaking in TE polarization was introduced by building and optimizing a set of SWs over the cylindrical surface. They are tailored to accept and carry the incident power on the lit side, and release a leaky wave that is amplitude and phase matched to the incident wave on the shadow side. The cloaking effectiveness was experimentally verified [30]. Furthermore, a modulated tensorial surface reactance distribution was numerically derived for impenetrable spherical surface cloaking [31].

Developing invisibility cloaking that functions for arbitrary polarization is desirable; however, it requires significant complexities in physical design and implementation compared with single-polarization scenarios. Polarization-insensitive carpet cloaking based on the TO has been reported by using a meta-atom that is insensitive to the polarization and incident angle [32] or by grouping simple meta-atoms that respond to different polarizations [33]. The scattering cancellation technique can be applied to cylindrical cloaking for dual polarization, using volumetric metamaterials [34,35] and FSSs [36,37].

In this paper, we introduce a thin printed metasurface on a grounded dielectric substrate, designed to conceal a large cylindrical object in all polarizations. In Sec. II, building on our previous work on the printed microwave cloak for TE polarization [30], the complete tangential TM fields incorporating an optimized set of auxiliary SWs are synthesized in a similar manner. The effect of a dielectric substrate is analyzed for different relative permittivities and thicknesses in Sec. III. Section IV shows that the optimized tensor surface reactances for both polarizations are physically realized using an array of modulated Jerusalem-cross-shaped meta-atoms. As an example design, a dual-polarized cylindrical metasurface cloak of a four-wavelength diameter at a microwave frequency is designed, fabricated, and experimentally characterized for the scattering characteristics. In Sec. V we show that the full-wave simulation of the physical metasurface predicts a significant scattering reduction for both polarizations. Section VI provides the verification of the simulation results with the experimental results of a fabricated cylindrical metasurface prototype. Section VII concludes the paper.

II. FIELD SYNTHESIS

The cross section of the proposed 2D dual-polarized metasurface cloaking configuration is illustrated in Fig. 1. With both the geometry and fields invariant in the z direction, let us consider an incident PW in an arbitrary polarization illuminating a PEC cylinder of radius a surrounded by a metasurface on a dielectric shell with a relative permittivity of ϵ_r. The outer and inner radii of the dielectric shell are a and $b = a - t$, respectively, where t is the thickness of the shell.

In an $e^{j\omega t}$ time convention, the time-harmonic incident PW propagating in the $+x$ direction can be linearly decomposed into TE and TM modes with the E field in the form $\mathbf{E}^i = \hat{z}E_z^i + \hat{y}E_y^i = (\hat{z}E_{\text{TE}}^i + \hat{y}E_{\text{TM}}^i)e^{-jkx}$ V/m, where E_{TE}^i and E_{TM}^i are amplitudes in TE and TM polarizations, respectively, and k is the free-space wave number. Utilizing auxiliary SWs, we follow the same cloaking principle validated for a single-polarized cylindrical metasurface cloak [30]. The metasurface accepts the incident PW and guides the power by converting it into SWs on the lit side
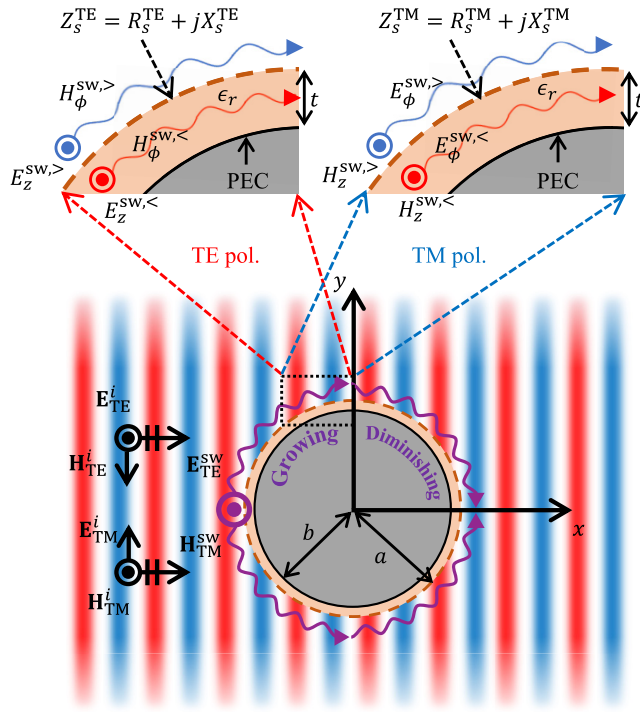
FIG. 1. A 2D configuration of dual-polarized metasurface cloaking. An incident PW propagates in the $+x$ direction and illuminates the cloaked PEC cylinder. Top: a magnified view of the SWs flowing conformally along the metasurface is illustrated for each polarization.

for each polarization. On the shadow side, the power of SWs is continuously leaked in the forward direction to recover the incident PW. Given that the TE and TM fields are decoupled under the z-invariance assumption [38],

i.e., (H_ρ, H_ϕ, E_z) for the TE mode and (E_ρ, E_ϕ, H_z) for the TM mode in standard cylindrical (ρ, ϕ, z) coordinates, we can address each polarization separately, and it is noted that the two modes are not duals of each other.

The TE- and TM-polarized SWs propagating in the direction of decreasing $|\phi|$ are built using the tangential E field at $\rho = a$, $E_{tz}^{\mathrm{sw}}(\phi) = E_z^{\mathrm{sw}}(\rho = a, \phi)$ and the tangential H field at $\rho = a^-$, $H_{tz}^{\mathrm{sw},-}(\phi) = H_z^{\mathrm{sw},<}(\rho = a^-, \phi)$, respectively. They are

$$E_{tz}^{\mathrm{sw}}(\phi) = \underbrace{E_1(\phi)e^{jk_c^{\mathrm{TE}}a|\phi|}}_{E_{1z}^{\mathrm{sw}}(\phi)} + \sum_{n=2}^{N_{\mathrm{TE}}} \underbrace{E_n(\phi)e^{j\psi_n^{\mathrm{TE}}(\phi)}}_{E_{nz}^{\mathrm{sw}}(\phi)}, \quad (1)$$

$$H_{tz}^{\mathrm{sw},-}(\phi) = \underbrace{H_1(\phi)e^{jk_c^{\mathrm{TM}}a|\phi|}}_{H_{1z}^{\mathrm{sw}}(\phi)} + \sum_{n=2}^{N_{\mathrm{TM}}} \underbrace{H_n(\phi)e^{j\psi_n^{\mathrm{TM}}(\phi)}}_{H_{nz}^{\mathrm{sw}}(\phi)}, \quad (2)$$

where $k_c^{\mathrm{TE/TM}}$ are the "carrier" propagation constants or the phase constants of the dominant SW terms selected in the invisible region (i.e., $k_c^{\mathrm{TE/TM}} > k$), $\psi_n^{\mathrm{TE/TM}}(\phi) = n\Delta\psi^{\mathrm{TE/TM}}(\phi) + \psi_0^{\mathrm{TE/TM}}(\phi)$, $\Delta\psi^{\mathrm{TE/TM}}(\phi) = k_c^{\mathrm{TE/TM}}a|\phi| - \psi_0^{\mathrm{TE/TM}}(\phi)$, and $\psi_0^{\mathrm{TE/TM}}(\phi) = \angle E_z^i$ or $\angle E_y^i$. In Eqs. (1) and (2), the envelope functions $E_1(\phi)$ and $H_1(\phi)$ represent the dominant SW terms, and they are real valued. The envelope functions $E_n(\phi)$ and $H_n(\phi)$ ($n = 2, \ldots, N_{\mathrm{TE/TM}}$) define higher-order SW terms, and they are chosen to be complex valued.

For the TM polarization, the z component of the H field associated with the SW inside the dielectric, $H_z^{\mathrm{sw},<}(\rho, \phi)$, can be expressed as a cylindrical harmonic expansion in terms of the tangential H field at $\rho = a$ on the dielectric side, $H_{tz}^{\mathrm{sw},-}(\phi)$, as

$$H_z^{\mathrm{sw},<}(\rho, \phi) = \sum_{n=-\infty}^{\infty} a_n \frac{H_n^{(1)}(k_d\rho)H_n^{(2)\prime}(k_db) - H_n^{(1)\prime}(k_db)H_n^{(2)}(k_d\rho)}{H_n^{(1)}(k_da)H_n^{(2)\prime}(k_db) - H_n^{(1)\prime}(k_db)H_n^{(2)}(k_da)} e^{jn\phi}, b \le \rho < a, \quad (3)$$

where $H_n^{(1)}(\cdot)$ and $H_n^{(2)}(\cdot)$ are the Hankel functions of order n of the first and second kinds, respectively, and a prime denotes differentiation with respect to the whole argument. In Eq. (3), $k_d = k\sqrt{\epsilon_r}$ is the wave number of the dielectric shell material and

$$a_n = \frac{1}{2\pi} \int_{-\pi}^{\pi} H_{tz}^{\mathrm{sw},-}(\phi)e^{-jn\phi}d\phi. \quad (4)$$

Using Maxwell's equations, one can find complete H_z- and E_ϕ-field components both inside and outside the dielectric associated with $H_{tz}^{\mathrm{sw},-}(\phi)$ in Eq. (2), noting the fact that E_ϕ is continuous across the penetrable metasurface at $\rho = a$. We find that

$$E_\phi^{\mathrm{sw},<}(\rho, \phi) = j\eta_d \sum_{n=-\infty}^{\infty} a_n \frac{H_n^{(1)\prime}(k_d\rho)H_n^{(2)\prime}(k_db) - H_n^{(1)\prime}(k_db)H_n^{(2)\prime}(k_d\rho)}{H_n^{(1)}(k_da)H_n^{(2)\prime}(k_db) - H_n^{(1)\prime}(k_db)H_n^{(2)}(k_da)} e^{jn\phi}, \quad b \le \rho \le a, \quad (5)$$

$$E_\phi^{\text{sw},>}(\rho,\phi) = j\eta_d \sum_{n=-\infty}^{\infty} a_n \frac{H_n^{(2)\prime}(k\rho)}{H_n^{(2)\prime}(ka)} G_n e^{jn\phi}, \qquad \rho \geq a,$$

$$\text{(6)}$$

$$H_z^{\text{sw},>}(\rho,\phi) = \frac{\eta_d}{\eta} \sum_{n=-\infty}^{\infty} a_n \frac{H_n^{(2)}(k\rho)}{H_n^{(2)\prime}(ka)} G_n e^{jn\phi}, \qquad \rho > a,$$

$$\text{(7)}$$

where

$$G_n = \frac{H_n^{(1)\prime}(k_d a) H_n^{(2)\prime}(k_d b) - H_n^{(1)\prime}(k_d b) H_n^{(2)\prime}(k_d a)}{H_n^{(1)}(k_d a) H_n^{(2)\prime}(k_d b) - H_n^{(1)\prime}(k_d b) H_n^{(2)}(k_d a)}. \quad \text{(8)}$$

The intrinsic impedances of free space and the dielectric are $\eta = \sqrt{\mu_0/\epsilon_0}$ and $\eta_d = \eta/\sqrt{\epsilon_r}$, respectively, where μ_0 and ϵ_0 are the free-space permeability and permittivity. The discontinuity of H_z across the impedance surface at the dielectric-air interface, $\Delta H_{tz}^{\text{sw}}(\phi) = H_{tz}^{\text{sw},+}(\phi) - H_{tz}^{\text{sw},-}(\phi) = H_z^{\text{sw},>}(\rho = a^+, \phi) - H_z^{\text{sw},>}(\rho = a^-, \phi)$, may cause power loss or gain at each point of the metasurface when the real part of the differential Poynting vector $\Delta S_\rho^{\text{TM}}(\phi) = \text{Re}\{E_{t\phi}^{\text{tot}}(\phi) \Delta H_{tz}^*(\phi)\}/2 = \text{Re}\{[E_{t\phi}^i(\phi) + E_{t\phi}^{\text{sw}}(\phi)][\Delta H_{tz}^i(\phi) + \Delta H_{tz}^{\text{sw}}(\phi)]^*\}/2$ is not equal to zero.

To obtain a pointwise passive and lossless metasurface, the tangential H field of the SW in TM polarization, $H_{tz}^{\text{sw},-}(\phi)$ in Eq. (2), is optimized to satisfy the locally and globally lossless condition at all points over the metasurface [39]. Specifically, the envelope functions, $H_n(\phi)$ ($n = 1, \ldots, N_{\text{TM}}$), are numerically optimized with the goal that the $\Delta S_{\rho,\text{TM}}(\phi)$ approach zero for all ϕ. Since this goal cannot be exactly achieved at all ϕ, we enforce the condition in an average sense. To that end, we define an error metric $e_{\text{sq}}^{\text{TM}}$ that quantifies how close the metasurface is to being lossless and gainless:

$$e_{\text{sq}}^{\text{TM}} = \frac{1}{e_0} \int_{-\pi}^{\pi} |\Delta S_\rho^{\text{TM}}(\phi)|^2 d\phi, \qquad \text{(9)}$$

$$e_0 = \int_{-\pi}^{\pi} |\Delta S_0^{\text{TM}}(\phi)|^2 d\phi, \qquad \text{(10)}$$

with $\Delta S_0^{\text{TM}}(\phi) = \text{Re}\{E_{t\phi}^i(\phi) \Delta H_{tz}^{i*}(\phi)\}/2$ the net outward Poynting vector component normal to the impedance surface associated with the incident PW. The optimization proceeds in the following steps.

(1) Optimize $H_1(\phi)$ so that the net Poynting vector component $\Delta S_1^{\text{TM}}(\phi) = \text{Re}\{E_{1\phi}^{\text{sw}}(\phi)[H_{1z}^{\text{sw},+}(\phi) - H_{1z}^{\text{sw},-}(\phi)]^*\}/2$ of the dominant SW term pointwise cancels out $\Delta S_0^{\text{TM}}(\phi)$.

(2) Optimize $H_n(\phi)$ ($n = 2, 3, \ldots, N_{\text{TM}}$) to minimize $e_{\text{sq}}^{\text{TM}}$ with $H_1(\phi)$ determined in step (1).

The optimization is carried out using the *fminsearch* function in MATLAB®.

Once $e_{\text{sq}}^{\text{TM}}$ reaches a sufficiently low threshold, the optimized tangential H field of the auxiliary SWs is determined via Eq. (2). The associated surface impedance for TM polarization is retrieved using the optimized tangential fields as

$$Z_s^{\text{TM}}(\phi) = R_s^{\text{TM}}(\phi) + jX_s^{\text{TM}}(\phi)$$

$$= -\frac{E_{t\phi}^i(\phi) + E_{t\phi}^{\text{sw}}(\phi)}{\Delta H_{tz}^i(\phi) + \Delta H_{tz}^{\text{sw}}(\phi)}. \quad \text{(11)}$$

Since the total tangential fields are optimized to satisfy the lossless condition, the surface resistance $R_s^{\text{TM}}(\phi)$ should be approximately equal to zero for all ϕ.

In this work, we only detail the synthesis of the TM-polarized SWs. The surface impedance for TE polarization, $Z_s^{\text{TE}} = R_s^{\text{TE}} + jX_s^{\text{TE}}$, can be found via the TE SW synthesis process reported in Ref. [30]. While the design approach stays unchanged for TE polarization, it is noted that the physical meta-atom design is vastly different from an array of printed strips in Ref. [30] due to the dual-polarization requirement in this work.

III. ANALYSIS OF THE EFFECT OF THE DIELECTRIC SUBSTRATE

In this section, case studies are presented for dielectrics of different relative permittivities and thicknesses on the surface reactance. Understanding how the dielectric shells affect the surface reactance distribution in different polarizations is beneficial when selecting an appropriate dielectric to implement the metasurface. The target frequency is 10 GHz, and the radius of the target object is $b = 60.33$ mm $\approx 2\lambda$ (where λ is the free-space wavelength), which is depicted as a PEC cylinder in Fig. 1. Here, the carrier propagation constants for both polarizations are selected to be $k_c^{\text{TE/TM}} = 2k$.

As demonstrated in Ref. [30], the surface reactances $X_s^{\text{TE/TM}}$ are expected to exhibit oscillations varying with position for cloaking purposes. The surface reactance modulation occurs around the unmodulated impedances $Z_{s0}^{\text{TE/TM}} = R_{s0}^{\text{TE/TM}} + jX_{s0}^{\text{TE/TM}}$ that support the dominant SWs (E_{1z}^{sw} and H_{1z}^{sw}) for the two polarizations. Thus, $Z_{s0}^{\text{TE/TM}}$ can be estimated from the transverse resonance condition in the radial direction at the impedance surface, derived as

$$X_{s0}^{\text{TE}} = \text{Im}\left\{\left[-\frac{j}{\eta} \frac{H_{k_c a}^{(2)\prime}(ka)}{H_{k_c a}^{(2)}(ka)} + \frac{jF_{k_c a}}{\eta_d}\right]^{-1}\right\}, \quad \text{(12)}$$

$$X_{s0}^{\text{TM}} = \text{Im}\left\{\left[\frac{j}{\eta} \frac{H_{k_c a}^{(2)}(ka)}{H_{k_c a}^{(2)\prime}(ka)} - \frac{j}{\eta_d G_{k_c a}}\right]^{-1}\right\}, \quad \text{(13)}$$

where

$$F_n = \frac{H_n^{(1)\prime}(k_d a) H_n^{(2)}(k_d b) - H_n^{(1)}(k_d b) H_n^{(2)\prime}(k_d a)}{H_n^{(1)}(k_d a) H_n^{(2)}(k_d b) - H_n^{(1)}(k_d b) H_n^{(2)}(k_d a)}. \quad \text{(14)}$$
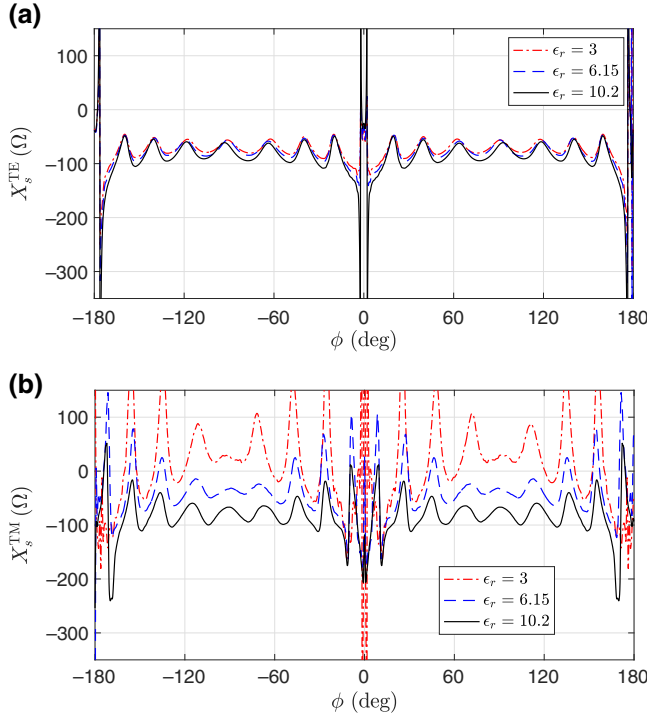
FIG. 2. Optimized distributions of $X_s(\phi)$ for the metasurface cloak for different relative permittivities $\epsilon_r = 3$, 6.15, and 10.2, designed to conceal a conducting cylinder with a radius of 2λ at 10 GHz. The thickness t of the dielectric shell is fixed at 1.27 mm. (a) TE polarization. (b) TM polarization.
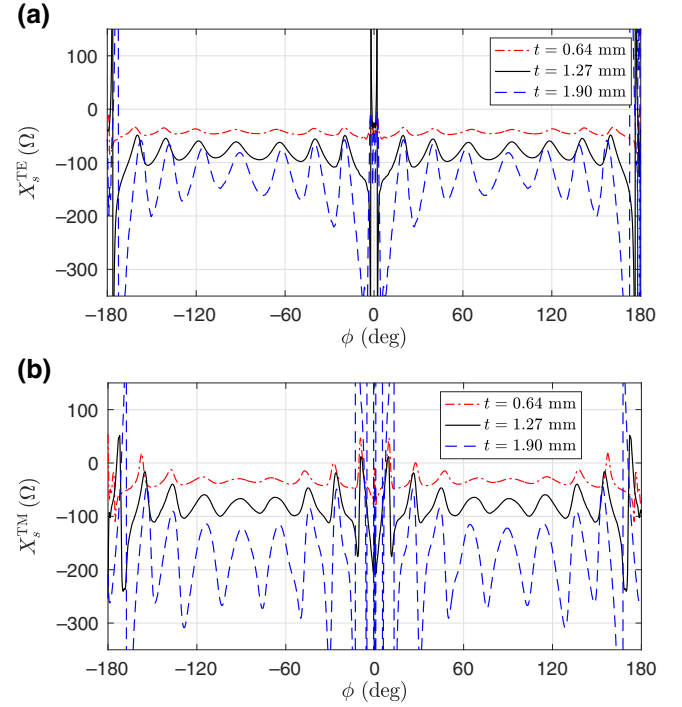

FIG. 3. Optimized distributions of $X_s(\phi)$ for the metasurface cloak for different substrate thicknesses $t = 0.64$, 1.27, and 1.9 mm, designed to conceal a conducting cylinder with a radius of 2λ at 10 GHz. The relative permittivity ϵ_r of the dielectric shell is fixed at 10.2. (a) TE polarization. (b) TM polarization.

Figure 2 plots the optimized X_s^{TE} and X_s^{TM} with respect to position for different relative permittivities $\epsilon_r = 3$, 6.15, and 10.2, when the thickness is fixed at $t = 1.27$ mm. In each scenario, the optimization successfully reduces $e_{\text{sq}}^{\text{TE/TM}}$ to a value lower than 10^{-3}, so that $R_s^{\text{TE/TM}}$ remains sufficiently close to zero and can thus be ignored. As shown in Fig. 2(a), despite varying ϵ_r, the X_s^{TE} oscillations remain within the range $[-110, -50]$ Ω. This aligns with the calculated X_{s0}^{TE} from Eq. (12), which are similar across $\epsilon_r = 3$, 6.15, and 10.2, at -68.20, -71.85, and -77.36 Ω, respectively. In the case of TM polarization, the approximate X_{s0}^{TM} values calculated from Eq. (13) show a significant variation, shifting from 33.18 to -37.04 and -78.16 Ω as ϵ_r increases. The resulting optimized X_s^{TM} are plotted in Fig. 2(b), where, unlike in the TE cases, the oscillation range varies noticeably with ϵ_r, fluctuating around the anticipated X_{s0}^{TM} values. It is observed that, with an increase in ϵ_r, the X_{s0}^{TM} distribution shifts toward capacitive values, and the reactance swings become narrower.

The impact of the dielectric thickness t on X_s is examined in Fig. 3, where the dielectric constant is fixed at $\epsilon_r = 10.2$, and $X_s^{\text{TE/TM}}$ are evaluated for three different thicknesses: $t = 0.64$, 1.27, and 1.9 mm. For the TE

polarization, X_s^{TE} shown in Fig. 3(a) exhibits oscillations within the capacitive range across the entire angular range. The center values of the oscillations are aligned approximately with predictions from Eq. (12): $X_{s0}^{\text{TE}} = -42.57$, -77.36, and -113.6 Ω for $t = 0.64$, 1.27, and 1.9 mm, respectively. A thicker dielectric layer leads to a more capacitive X_s^{TE} distribution and a wider oscillation range. For the TM polarization, the optimized X_s^{TM} for different dielectric thicknesses are plotted in Fig. 3(b). The center of the oscillation shifts towards the negative value with a thicker dielectric shell. This closely matches the estimated $X_{s0}^{\text{TM}} = -33.14$, -78.16, and -166.37 Ω for $t = 0.64$, 1.27, and 1.90 mm, respectively. Similar to the TE case, a thicker dielectric induces a larger reactance swing.

In the two case studies, it can be observed that X_s^{TM} is more sensitive to changes in the dielectric in both the permittivity and the thickness compared with X_s^{TE}. While X_s^{TE} consistently remains in the capacitive regime across all scenarios, X_s^{TM} can reach inductive values when the relative permittivity is low. For a prototype cloak for fabrication, we choose a dielectric shell with $\epsilon_r = 10.2$ and $t = 1.27$ mm, for which $X_s^{\text{TE}}(\phi)$ and $X_s^{\text{TM}}(\phi)$ exhibit similar ranges of surface reactance variation with respect to ϕ.

IV. PRINTED METASURFACE DESIGN

The synthesized anisotropic surface reactance tensor, with elements $X_s^{\text{TE}}(\phi)$ and $X_s^{\text{TM}}(\phi)$, is physically implemented using a meta-atom. We choose a modified Jerusalem-cross-patterned sheet conductor as the meta-atom, placed on a grounded dielectric substrate. As can be seen in Figs. 2 and 3, the required capacitive reactance ranges along the z and ϕ directions are different. Hence, we break the symmetry of the standard Jerusalem cross along the two arm directions, and introduce a central gap of g_{h2} only along the ϕ direction, as shown in Fig. 4(a). The modified Jerusalem-cross-patterned conductor sheet is capable of controlling its anisotropic surface reactance by adjusting the dimensions, with weak spatial dispersion [40]. Three parameters (d_h, g_{h2}, l_v) are selected as design parameters. In particular, the central gap g_{h2} is chosen among the three values of 0, 0.1, and 0.4 mm. The chosen ranges for the other parameters are $d_h \in [0.1, 1]$ mm and $l_v \in [g_{h2} + 0.2, 1.8]$ mm.

Unlike in previous works [30,40], the unit-cell dimension in the ϕ direction, $d_\phi = \lambda/10$, cannot be considered negligibly small relative to the radius $a = 2\lambda$. Thus, in this case, the tensorial surface reactance elements of the meta-atom, $X_{\phi\phi}$ and X_{zz}, are extracted by simulating a wedged-shaped sector waveguide, as shown in Fig. 4(b), which was introduced in Refs. [41,42]. Inside the sector waveguide, the meta-atom is illuminated by a circumferential zeroth-order TE- and TM-polarized converging cylindrical wave propagating towards the cylinder axis, respectively. The magnitude and phase of the outward-traveling, diverging cylindrical wave characterize the reflection property of the meta-atom. Then, using the reflection coefficients $\Gamma^{\text{TE/TM}}(d_h, g_{h2}, l_v)$ with respect to the design parameters obtained via COMSOL Multiphysics®, the penetrable surface impedance can be evaluated using the transverse resonance condition. It is expressed as

$$
\begin{aligned}
&Z_s^{\text{TE/TM}}(d_h, g_{h2}, l_v) \\
&= \left[\frac{1 - \Gamma^{\text{TE/TM}}(d_h, g_{h2}, l_v)}{1 + \Gamma^{\text{TE/TM}}(d_h, g_{h2}, l_v)} - \frac{1}{Z^{\text{TE/TM}}} \right]^{-1},
\end{aligned} \tag{15}
$$

where $Z^{\text{TE}} = j\eta_d F_0$ and $Z^{\text{TM}} = j\eta_d G_0$. For the chosen meta-atom, the values of Z^{TE} and Z^{TM} are calculated to be $j\,136.28$ and $j\,132.54\,\Omega$, respectively. For the three discrete values of g_{h2}, the retrieved $X_{\phi\phi}$ and X_{zz} with respect to d_h and l_v are plotted for each polarization in Figs. 4(c)–4(h). As can be expected, d_h and g_{h2} predominantly affect $X_{\phi\phi}$, and the values of X_{zz} depend mostly on l_v. Nonetheless, there are weak dependencies of $X_{\phi\phi}$ on l_v and of X_{zz}
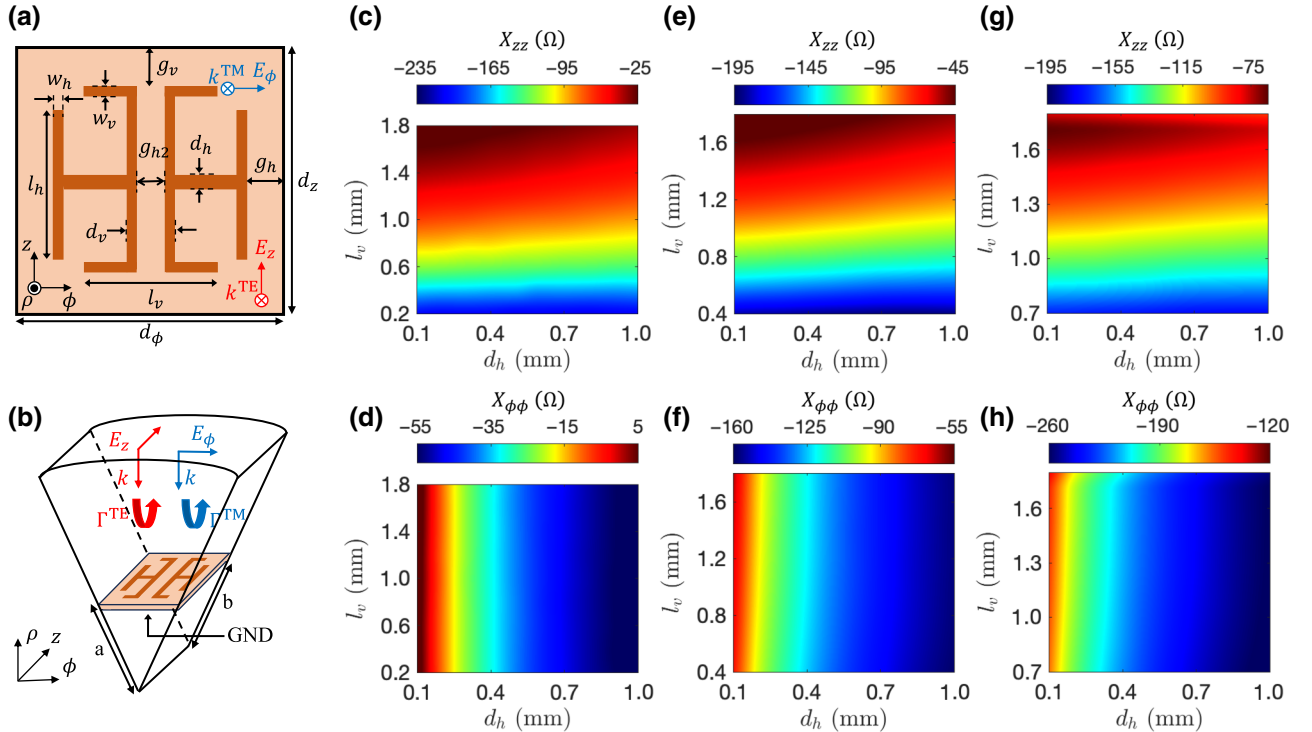

FIG. 4.   Printed meta-atom design for surface reactance realization for the two polarizations. (a) Top view of a unit cell having a printed Jerusalem cross with a vertical gap in the ϕ direction. There are three design parameters: d_h, g_{h2}, and l_v. The gap g_{h2} is selected among 0, 0.1, and 0.4. Fixed dimensions are as follows: $d_z = 3$, $d_\phi = 3$, $l_h = 1.8$, $g_h = 0.05$, $w_h = 0.1$, $d_v = g_{h2} + 0.3$, $w_v = 0.1$, $g_v = 0.05$. (b) A meta-atom inside a wedged-plate cylindrical waveguide. (c) The X_{zz} for $g_{h2} = 0$. (d) The $X_{\phi\phi}$ for $g_{h2} = 0$. (e) The X_{zz} for $g_{h2} = 0.1$. (f) The $X_{\phi\phi}$ for $g_{h2} = 0.1$. (g) The X_{zz} for $g_{h2} = 0.4$. (h) The $X_{\phi\phi}$ for $g_{h2} = 0.4$. Units for all lengths are millimeters.
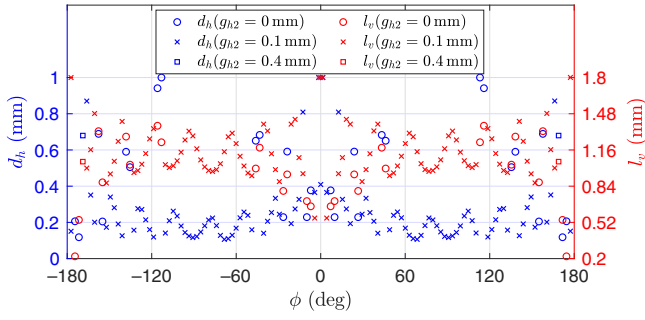
FIG. 5. Design parameters for the optimized physical metasurface design for dual-polarized cylindrical cloaking of a 2λ-radius cylinder.

on d_h and g_{h2}. Hence, simultaneous consideration of the three design parameters is necessary to realize a given pair of reactances $[X_s^{\text{TE}}(\phi), X_s^{\text{TM}}(\phi)]$. The design maps cover most of the required tensor surface reactance values, except for some points near $\phi = 0$ and π, where the reactance values are extreme.

In the meta-atom design, introduction of the gap g_{h2} extends the range of achievable $X_{\phi\phi}$ beyond what can be realized by varying d_h alone, and they are the two main design parameters for $X_{\phi\phi}$. Consequently, the total range of $X_{\phi\phi}$ is the union of three distinct ranges [see the three color axes in Figs. 4(d), 4(f), and 4(h)]. Furthermore, we choose to keep the size and location of the end loads along the reactance modulation direction—the strips of dimensions $l_h \times w_h$—fixed. Using only "interior" dimensions as design parameters ensures that the capacitive coupling between neighboring meta-atoms along the modulation direction remains relatively unchanged from the prediction made using the unit-cell analysis. On the other hand, there is no reactance modulation in the z direction. So, we choose the length of the broken-strip end load, l_v, as the main design parameter for X_{zz}. It can adjust X_{zz} in a wide range [see the color axes in Figs. 4(c), 4(e), and 4(g)].

The required pair $[X_{zz}(\phi), X_{\phi\phi}(\phi)]$ is discretized at an interval of d_ϕ/a in ϕ and matched with the available pair $[X_s^{\text{TE}}(\phi), X_s^{\text{TM}}(\phi)]$ from the unit-cell analysis to find the design parameters (d_h, g_{h2}, l_v) within the design domain. As a result, 129 meta-atoms are arranged along the circumference, and the selected design parameters are plotted in Fig. 5. Except for extreme surface reactances, design parameters for a vast majority of the required anisotropic reactance values are found.

V. SIMULATION RESULTS

The bare PEC cylinder and 3D printed modified Jerusalem-cross array covering the PEC cylinder are modeled and simulated using COMSOL Multiphysics. Figures 6(a) and 6(b) show snapshots of the total E_z distribution in the x-y plane, Re $\{E_z(x,y)\}$, as a TE-polarized

incident wave with $\mathbf{E}^i = \hat{z}e^{-jkx}$ V/m impinges on PEC cylinders of a 4λ diameter without and with the printed metasurface cloak, respectively. For the bare cylinder, a strong scattered field is seen around the cylinder. Notably, we can see a wide shadow region with negligible field near $\phi = 0$. For the cloaked cylinder, a strong SW is observed bound to and traveling along the perimeter of the cloak [inset of Fig. 6(b)] as the power of the incident wave is continuously accepted on the lit side, as intended. On the shadow side, the SW power is continuously leaked in the forward direction, reconstructing the incident field. Backward scattering is observed near $\phi = \pi$. However, relative to the bare cylinder scenario, the overall field distribution is close to that of the incident wave.

Figures 6(c) and 6(d) display snapshots of the H-field distribution, $H_z(x,y)$, when a TM-polarized incident wave with $\mathbf{E}^i = \hat{y}e^{-jkx}$ V/m impinges on the bare PEC and cloaked cylinder, respectively. Similarly to the TE case, while strong scattered waves around the bare PEC cylinder are observed, the metasurface cloak mitigates the field scattering in all directions. As intended, SWs in TM polarization are induced [inset of Fig. 6(d)], propagating along the printed patterned surface. The magnitude of the restored propagating wave in the shadow region is close to that of the incident wave, much greater than in the bare cylinder scenario.

To assess the conversion effectiveness of the incident PW into SWs across the illuminated side, we define the power conversion efficiency as a ratio of the power carried across the y-z plane in the $+x$ direction while tightly bound to the metasurface cloak to the incident power over the cylinder cross section as

$$e_{\text{coup}}^{\text{TE/TM}} = \frac{\int_0^{d_z} \int_b^{y_1} S_x^{\text{TE/TM}}(x=0)dydz}{\int_0^{d_z} \int_0^{y_1} (1/2) \, \text{Re} \left\{ \mathbf{E}^i \times \mathbf{H}^{i*} \right\} dydz}, \quad (16)$$

where $y_1 = b + 8.25 = 68.58$ mm is the y position at which the dominant SW field term exponentially decays to -30 dB from the value on the metasurface at $x = 0$. A mirror symmetry with respect to $y = 0$ has been used in defining $e_{\text{coup}}^{\text{TE/TM}}$. The numerator in Eq. (16) can be numerically evaluated using COMSOL Multiphysics, and the denominator is equal to $y_1 d_z/2\eta$ for the given incident fields for both polarizations. The TE efficiency $e_{\text{coup}}^{\text{TE}}$ is evaluated to be 0.9815 for the numerically enforced $X_s^{\text{TE}}(\phi)$ and 0.7785 for the physical metasurface cloak. In the case of TM polarization, $e_{\text{coup}}^{\text{TM}}$ is calculated to be 0.9338 and 0.7570 for the numerical reactance surface of $X_s^{\text{TM}}(\phi)$ and the physical metasurface, respectively. The efficiency figures in excess of 90% validates the reactance surface synthesis for PW-SW conversion via field optimization. The physical metasurface as a modulated array of discrete meta-atoms achieves the envisioned conversion at slightly reduced efficiencies.
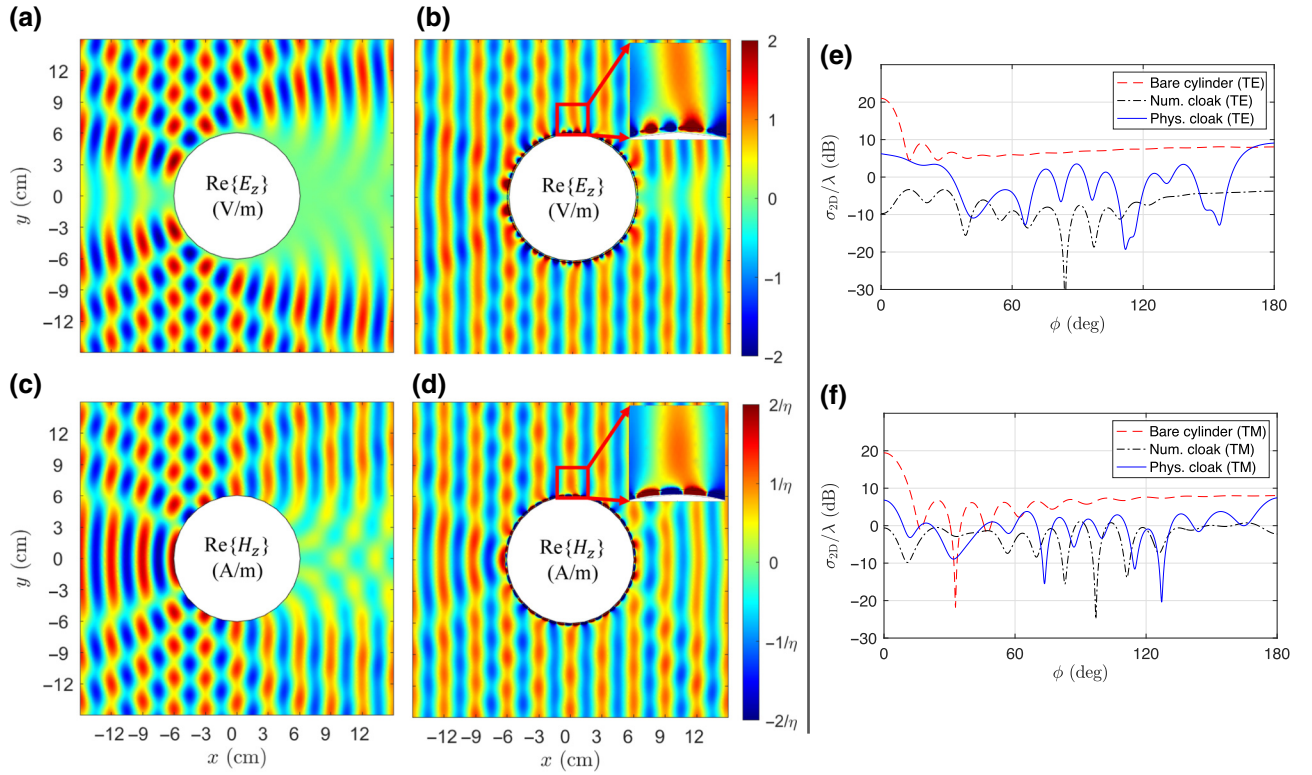
FIG. 6. Three-dimensional simulation results for scattering scenarios with bare and cloaked 4λ-diameter PEC cylinders for the two polarizations. Snapshots of the total $E_z(x,y)$ distribution for (a) the bare PEC cylinder and (b) the cloaked cylinder in TE polarization. Snapshots of the total $H_z(x,y)$ distribution for (c) the bare PEC cylinder and (d) the cloaked cylinder in TM polarization. The insets of (b) and (d) show magnified views of the near the topmost parts of the cloak for each polarization. Comparison of the 2D bistatic RCS between the bare PEC cylinder, the numerical cloak, and the physical cloak in (e) TE and (f) TM polarizations.

In Figs. 6(e) and 6(f), 2D bistatic radar cross sections (RCSs) or scattering widths normalized by the wavelength at 10 GHz, σ_{2D}/λ, are compared over $\phi \in [0, \pi]$ between a bare PEC cylinder, a penetrable surface cloak with a numerically enforced surface reactance profile $X_s^{\text{TE/TM}}(\phi)$, and the physical metasurface cloak in TE and TM polarizations, respectively. The 2D RCS profiles over $\phi \in [-\pi, 0]$ are symmetric about $\phi = 0$ relative to those over $\phi \in [0, \pi]$. In the TE polarization [Fig. 6(e)], it can be seen that the numerical and physical cloak designs reduce the RCS in most directions relative to the PEC cylinder case. In particular, the RCSs in the forward direction $\sigma_{2D}(\phi = 0)/\lambda$ drop by 30.78 and 14.79 dB with the numerical and physical cloaks, respectively. To gauge the overall cloaking performance, the total scattering cross section (SCS) is defined by integrating σ_{2D} with respect to the angle [43,44] as

$$\sigma_{2D}^{\text{tot}} = \frac{1}{2\pi} \int_{-\pi}^{\pi} \sigma_{2D}(\phi) d\phi. \qquad (17)$$

From Eq. (17), σ_{2D}^{tot} decreases by 15.96 and 7.67 dB for the numerical and physical cloak scenarios, respectively, compared with the PEC cylinder case. The RCS increase for

the physical cloak in comparison with the numerical one is due mainly to the discretization of the reactance profile and the distinctly different neighboring meta-atoms in close proximity around $\phi = 0$ and π. Although the backward scattering at $\phi = \pi$ for the physical cloak is slightly higher than that of the bare cylinder, the total SCS remains smaller.

In Fig. 6(f), for the TM polarization, a similar trend of RCS reduction as in the TE polarization for cloaked cylinders compared with the bare PEC cylinder scenario is observed. For the bare cylinder, a stronger angular RCS variation takes place due to the creeping waves in TM polarization. For the numerical and physical cloaks, forward scattering is decreased by 20.06 and 12.64 dB, and the total SCS is reduced by 10.67 and 7.58 dB, respectively. The cloaking performance of the physical metasurface cloak is slightly inferior to the numerical cloak it aims to achieve, as in the TE polarization case.

In Fig. 7, the 2D RCS patterns of the printed metasurface cloak under oblique PW illumination are examined for both polarizations, compared with the bare cylinder scenarios. For TE polarization, the RCS patterns are shown in Fig. 7(a), where a PW with the incident E field $\mathbf{E}_{\text{TE}}^i(x,z) = (\hat{x} \sin \theta^i + \hat{z} \cos \theta^i) E_0 e^{-jk(x \cos \theta^i - z \sin \theta^i)}$
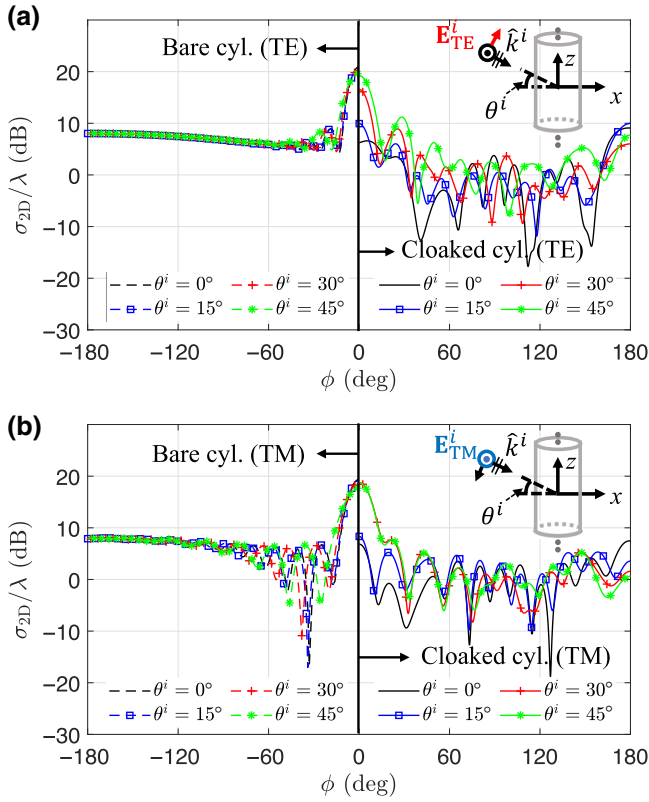
FIG. 7. Simulated 2D bistatic RCSs of a bare cylinder and the printed metasurface cloak for incident PWs with an oblique incident angle θ^i. (a) Two-dimensional RCS for TE polarization (equivalent to the TM-to-z polarization). (b) Two-dimensional RCS for TM polarization (equivalent to the TE-to-z polarization). For both polarizations, the RCSs for the bare and cloaked cylinders are plotted over $\phi \in [-\pi, 0]$ and $\phi \in [0, \pi]$, respectively. The RCS in each scenario has a mirror symmetry with respect to $\phi = 0$.

impinges on the cloak. In addition to normal incidence ($\theta^i = 0°$), investigations are conducted for angles of incidence $\theta^i = 15°, 30°$, and $45°$. As θ^i deviates from $0°$, the RCS of the cloak increases in overall directions with a particularly noticeable increase in the forward RCS ($\phi = 0$). When $\theta^i = 45°$, the forward RCS value is comparable to that of the bare cylinder. Figure 7(b) shows the RCS for a TM-polarized incident PW with incident angle θ^i, associated with the E field $\mathbf{E}_{TM}^i(x, z) = -\hat{y}E_0 e^{-jk(x\cos\theta^i - z\sin\theta^i)}$. At $\theta^i = 15°$, the RCS of the cloaked cylinder maintains low values, comparable to the normal incidence case. However, for $\theta^i \geq 30°$, there are significant increases in the RCS in the forward direction. The RCS increase under oblique incident waves occurs because the cloak designed for normally incident TE- and TM-polarized waves no longer effectively restores the incident wave behind the cylinder. Such oblique incidences result in a hybrid mode, and the local lossless condition at a metasurface point does not split into two decoupled conditions for individual

polarizations, as it does for normal incidence. As a result, cloak design under an oblique incidence is more involved, and it is also a function of the incident polarization.

VI. EXPERIMENTAL RESULTS

The physical metasurface design is fabricated using Rogers RO6010.2 laminates, and measured in the anechoic chamber for its scattering characteristics. The overall measurement setup is shown in Fig. 8(a). Covering a 4λ-diameter aluminum cylinder, the metasurface prototype of a 40-cm length in the z direction is suspended in the air using a fishing line attached to a wooden stand. We also measured the bare cylinder and the free-space scenarios in separate measurements. A network analyzer measures S_{21} between a standard horn transmitting (TX) antenna and a small receiving (RX) horn antenna mounted on a rotation stage [Fig. 8(b)]. The separation between the cylindrical scatterer and the RX antenna is 90 cm, approximately corresponding to the starting distance of the Franhofer zone. The RX horn always faces the scatterer. The range of the angle ϕ that can be measured is $\phi \in [-160°, 160°]$, with $\phi = 0$ corresponding to the forward scattering direction (i.e., from the TX antenna toward the cylinder axis). The
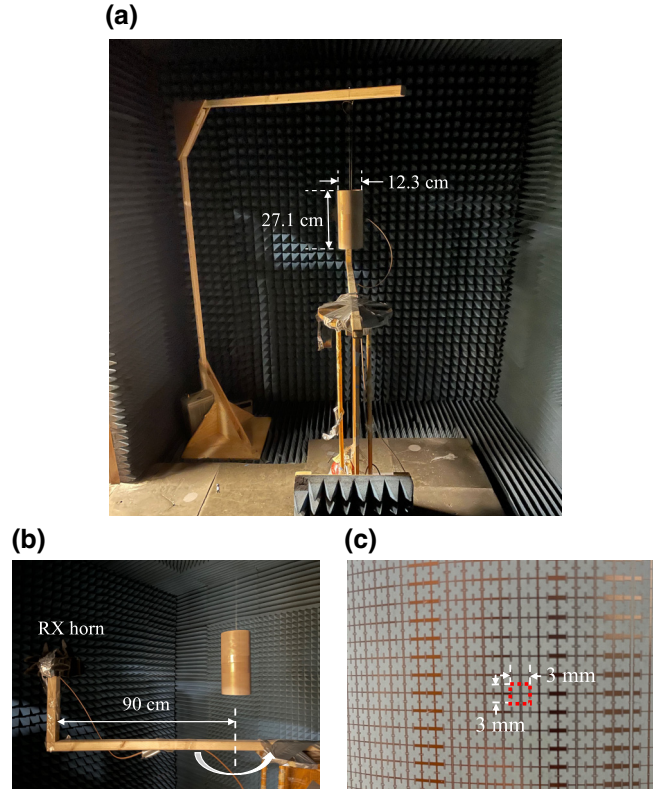

FIG. 8. Scattering measurement of the metasurface cloak prototype. (a) Measurement setup in a radio anechoic chamber. (b) The suspended cloak prototype and the RX horn antenna fixed on a rotation stage. (c) A close-up view of the fabricated printed metasurface cloak.

TX horn antenna is located behind the spot where the photo in Fig. 8(a) is taken, radiating a linearly polarized wave in either the vertical or horizontal direction toward the scatterer. To mitigate scattering from the RX antenna body when $\phi \approx \pm 160°$, the sides and back of the RX horn antenna are covered with microwave absorbers. Figure 8(c) shows a magnified view of the metasurface prototype, wrapped around the aluminum cylinder. It is a printed array of patterned Jerusalem-cross copper cladding, modulated along the cylinder circumference and periodic along the cylinder axis direction.

Figure 9 plots the measured bistatic scattering, characterized by $S_{21}(\phi)$ on a decibel scale after normalization by $\max_{\phi} |S_{21}(\phi)|$ of the free-space scenario for each polarization. In the case of TE polarization, Fig. 9(a) represents the normalized $S_{21}^{TE}(\phi)$ at 10.03 GHz. In the free-space case (i.e., absence of the scatterer), the measured pattern is essentially the radiation pattern of the RX horn antenna with respect to ϕ. For the bare PEC cylinder scenario, scattering occurs in all directions, resulting in a larger $|S_{21}|$ compared with the free-space scenario. The only exception is the shadow region behind the cylinder near $\phi = 0$. Blockage by the 4λ-across aluminum cylinder reduces the total field measured by the RX antenna. On the other hand, with the metasurface cloak applied to the same conductor cylinder, scattering occurs to a lesser extent, scattering

reduces in all directions, and the measured field closely approaches the free-space pattern. However, this scattering elimination by the cloak is not perfect, as can be observed by deviations near $\phi = 0$ and $160°$ due to imperfections in the physical metasurface compared with the numerical design. The field strength for the cloaked cylinder is close to the free-space case and higher by 4.94 dB at $\phi = 0$ than the base cylinder case, confirming that the incident wave is properly restored in the shadow region. For the TM polarization, the measured normalized $S_{21}^{TM}(\phi)$ at 10.08 GHz is plotted in Fig. 9(b). A trend similar to the TE polarization is observed. At $\phi = 0$, the measured total field with the cloak is close to the no-scatterer case and is 4.80 dB higher than without the cloak. The frequency deviation for most scattering reduction from the design frequency of 10.0 GHz in both polarizations may be attributed to variations in fabrication tolerances and imperfections in the measurement setup. Nonidealities include a finite length in the z direction for the scatterer and cloak as well as the incident wave by the TX horn not exactly being a PW.

The forward restoration level (FRL) is defined as $|S_{21,\text{cloaked/uncloaked}}(\phi = 0)/S_{21,\text{freespace}}(\phi = 0)|$ on a decibel scale and plotted in Fig. 10 with respect to the frequency for both TE and TM polarizations. Perfect cloaking results in FRL = 0 dB. The 3-dB FRL bandwidths, which correspond to the frequency ranges up to 3 dB below the FRL peak values in the cloaked scenarios, are
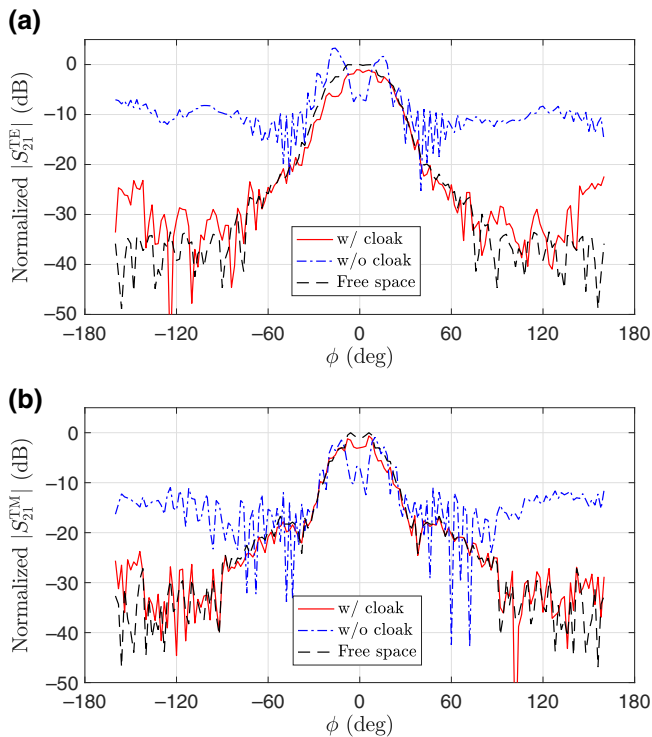

FIG. 9. Normalized scattering responses for three different scenarios: the bare aluminum cylinder, the cloaked cylinder, and no cylinder. (a) TE polarization at 10.03 GHz. (b) TM polarization at 10.08 GHz.
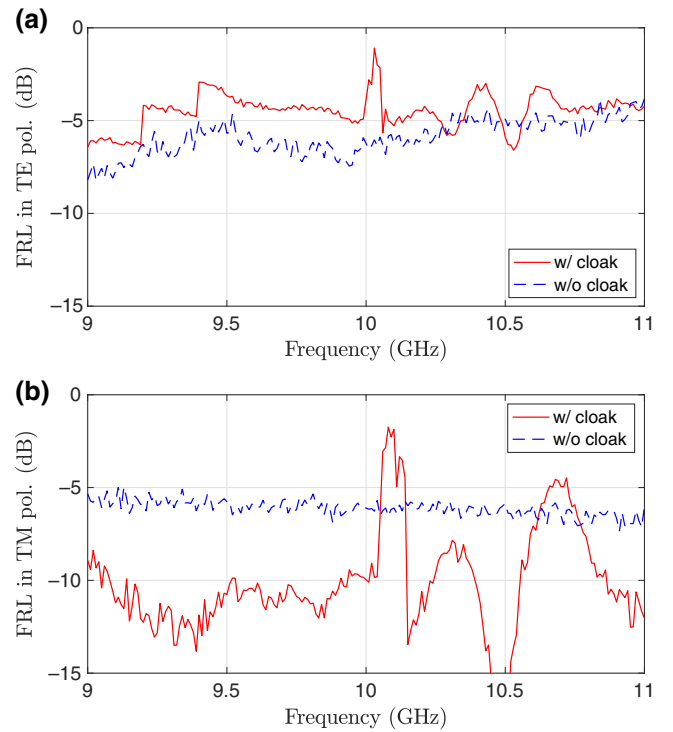

FIG. 10. Forward restoration level with respect to the frequency, defined by $|S_{21,\text{cloaked/uncloaked}}(\phi = 0)/S_{21,\text{freespace}}(\phi = 0)|$ on a decibel scale for (a) TE and (b) TM polarizations.

0.5% (10.00–10.05 GHz) for the TE polarization and 0.4% (10.06–10.10 GHz) for the TM polarization. A deviation from the target frequency leads to an increased magnitude or phase error for the reconstructed incident wave in the shadow region. A mismatch between the accumulated phases across the cylinder diameter for the incident plane wave and the SW along the conformal metasurface results in an inherently narrow cloaking bandwidth.

VII. CONCLUSION

A unidirectional printed metasurface cylindrical cloak effective for both TE and TM polarizations has been designed and demonstrated. To achieve the invisibility cloaking ability, the total tangential fields on the penetrable impedance surface are synthesized using auxiliary SWs optimized to satisfy the locally and globally lossless and gainless condition for each polarization. The distribution of anisotropic penetrable surface reactance is physically realized as a modulated array of modified Jerusalem-cross-shaped meta-atoms on a grounded cylindrical dielectric shell. A numerical study on the permittivity and thickness of the dielectric substrate demonstrates how the choice of the dielectric substrate affects the surface reactance for each polarization. The dual-polarized printed metasurface cloak is capable of concealing a large free-standing object as a thin and easy-to-fabricate structure for an incident PW of an arbitrary polarization.

ACKNOWLEDGMENTS

[1] J. B. Pendry, D. Schurig, and D. R. Smith, Controlling electromagnetic fields, Science **312,** 1780 (2006).

[2] D. H. Werner and D.-H. Kwon, *Transformation Electromagnetics and Metamaterials* (Springer, London, UK, 2013).

[3] D. Schurig, J. J. Mock, B. J. Justice, S. A. Cummer, J. B. Pendry, A. F. Starr, and D. R. Smith, Metamaterial electromagnetic cloak at microwave frequencies, Science **314,** 977 (2006).

[4] N. Landy and D. R. Smith, A full-parameter unidirectional metamaterial cloak for microwaves, Nat. Mater. **12,** 25 (2013).

[5] C.-W. Qiu, L. Hu, X. Xu, and Y. Feng, Spherical cloaking with homogeneous isotropic multilayered structures, Phys. Rev. E **79,** 047602 (2009).

[6] R. Liu, C. Ji, J. J. Mock, J. Y. Chin, T. J. Cui, and D. R. Smith, Broadband ground-plane cloak, Science **323,** 366 (2009).

[7] A. Alù, Mantle cloak: Invisibility induced by a surface, Phys. Rev. B **80,** 245115 (2009).

[8] B. Edwards, A. Alù, M. G. Silveirinha, and N. Engheta, Experimental verification of plasmonic cloaking at microwave frequencies with metamaterials, Phys. Rev. Lett. **103,** 153901 (2009).

[9] J. Soric, P. Chen, A. Kerkhoff, D. Rainwater, K. Melin, and A. Alù, Demonstration of an ultralow profile cloak for scattering suppression of a finite-length rod in free space, New J. Phys. **15,** 033037 (2013).

[10] P.-Y. Chen and A. Alu, Mantle cloaking using thin patterned metasurfaces, Phys. Rev. B **84,** 205110 (2011).

[11] Y. R. Padooru, A. B. Yakovlev, P.-Y. Chen, and A. Alù, Analytical modeling of conformal mantle cloaks for cylindrical objects using sub-wavelength printed and slotted arrays, J. Appl. Phys. **112,** 034907 (2012).

[12] A. Monti, L. Tenuti, G. Oliveri, A. Alù, A. Massa, A. Toscano, and F. Bilotti, in *8th Int. Congr. Adv. Electromagn. Mater. Microw. Opt. (Metamaterials 2014)* (IEEE, Copenhagen, Denmark, 2014), pp. 214–216, https://ieeexplore.ieee.org/document/6948651.

[13] X.-Y. Luo, W.-L. Guo, K. Chen, J. Zhao, T. Jiang, Y. Liu, and Y. Feng, Active cylindrical metasurface with spatial reconfigurability for tunable backward scattering reduction, IEEE Trans. Antennas Propag. **69,** 3332 (2021).

[14] P.-Y. Chen, C. Argyropoulos, and A. Alù, Broadening the cloaking bandwidth with non-Foster metasurfaces, Phys. Rev. Lett. **111,** 233001 (2013).

[15] S. Liu, H.-X. Xu, H. C. Zhang, and T. J. Cui, Tunable ultrathin mantle cloak via varactor-diode-loaded metasurface, Opt. Express **22,** 13403 (2014).

[16] P.-Y. Chen and A. Alu, Atomically thin surface cloak using graphene monolayers, ACS Nano **5,** 5855 (2011).

[17] P.-Y. Chen, M. Farhat, S. Guenneau, S. Enoch, and A. Alù, Acoustic scattering cancellation via ultrathin pseudo-surface, Appl. Phys. Lett. **99,** 191913 (2011).

[18] D. A. Miller, On perfect cloaking, Opt. Express **14,** 12457 (2006).

[19] F. G. Vasquez, G. W. Milton, and D. Onofrei, Active exterior cloaking for the 2D Laplace and Helmholtz equations, Phys. Rev. Lett. **103,** 073901 (2009).

[20] D. L. Sounas, R. Fleury, and A. Alù, Unidirectional cloaking based on metasurfaces with balanced loss and gain, Phys. Rev. Appl. **4,** 014005 (2015).

[21] M. Selvanayagam and G. V. Eleftheriades, Experimental demonstration of active electromagnetic cloaking, Phys. Rev. X **3,** 041011 (2013).

[22] P. Ang and G. V. Eleftheriades, An active electromagnetic 3-D surface cloak, IEEE Trans. Antennas Propag. **71,** 1765 (2022).

[23] C. L. Holloway, E. F. Kuester, J. A. Gordon, J. O'Hara, J. Booth, and D. R. Smith, An overview of the theory and applications of metasurfaces: The two-dimensional equivalents of metamaterials, IEEE Antennas Propag. Mag. **54,** 10 (2012).

[24] H. Chu, Q. Li, B. Liu, J. Luo, S. Sun, Z. H. Hang, L. Zhou, and Y. Lai, A hybrid invisibility cloak based on integration of transparent metasurfaces and zero-index materials, Light Sci. Appl. **7,** 50 (2018).

[25] G. Xu, G. V. Eleftheriades, and S. V. Hum, Approach to the analysis and synthesis of cylindrical metasurfaces with noncircular cross sections based on conformal transformations, Phys. Rev. B **102,** 245305 (2020).

[26] M. Dehmollaian, G. Lavigne, and C. Caloz, Transmit-table nonreciprocal cloaking, Phys. Rev. Appl. **19**, 014051 (2023).

[27] A. Epstein and G. V. Eleftheriades, Synthesis of passive lossless metasurfaces using auxiliary fields for reflection-less beam splitting and perfect reflection, Phys. Rev. Lett. **117**, 256103 (2016).

[28] D.-H. Kwon, Lossless tensor surface electromagnetic cloaking for large objects in free space, Phys. Rev. B **98**, 125137 (2018).

[29] H. Lee and D.-H. Kwon, Large and efficient unidirectional plane-wave–surface-wave metasurface couplers based on modulated reactance surfaces, Phys. Rev. B **103**, 165142 (2021).

[30] H. Lee and D.-H. Kwon, Microwave metasurface cloaking for freestanding objects, Phys. Rev. Appl. **17**, 054012 (2022).

[31] D.-H. Kwon, in *Proc. 2023 IEEE Int. Symp. Antennas Propag.* (IEEE, Portland, OR, 2023), pp. 577–578, https://ieeexplore.ieee.org/abstract/document/10238060.

[32] Y. Yang, L. Jing, B. Zheng, R. Hao, W. Yin, E. Li, C. M. Soukoulis, and H. Chen, Full-polarization 3D metasurface cloak with preserved amplitude and phase, Adv. Mater. **28**, 6866 (2016).

[33] H.-X. Xu, G. Hu, Y. Wang, C. Wang, M. Wang, S. Wang, Y. Huang, P. Genevet, W. Huang, and C.-W. Qiu, Polarization-insensitive 3D conformal-skin metasurface cloak, Light: Sci. Appl. **10**, 75 (2021).

[34] F. Bilotti, S. Tricarico, and L. Vegni, Electromagnetic cloaking devices for TE and TM polarizations, New J. Phys. **10**, 115035 (2008).

[35] V. I. Shcherbinin, Y. K. Moskvitina, V. I. Fesenko, and V. R. Tuz, Dual-polarized all-angle cloaking of a dielectric nanowire by helical graphene ribbons, Phys. Rev. B **100**, 035428 (2019).

[36] A. Monti, J. C. Soric, A. Alù, A. Toscano, and F. Bilotti, Anisotropic mantle cloaks for TM and TE scattering reduction, IEEE Trans. Antennas Propag. **63**, 1775 (2015).

[37] J. C. Soric, A. Monti, A. Toscano, F. Bilotti, and A. Alù, Dual-polarized reduction of dipole antenna blockage using mantle cloaks, IEEE Trans. Antennas Propag. **63**, 4827 (2015).

[38] R. F. Harrington, *Time-Harmonic Electromagnetic Fields* (Wiley-IEEE Press, Hoboken, NJ, 2001).

[39] A. Epstein and G. V. Eleftheriades, Arbitrary power-conserving field transformations with passive lossless omega-type bianisotropic metasurfaces, IEEE Trans. Antennas Propag. **64**, 3880 (2016).

[40] H. Lee and D.-H. Kwon, 2-D circularly polarized printed metasurface leaky-wave antennas on a conformal aperture, IEEE Antennas Wireless Propag. Lett. **22**, 2614 (2023).

[41] G. Xu, G. V. Eleftheriades, and S. V. Hum, Discrete-Fourier-transform-based framework for analysis and synthesis of cylindrical omega-bianisotropic metasurfaces, Phys. Rev. Appl. **14**, 064055 (2020).

[42] J. Li, A. Díaz-Rubio, C. Shen, Z. Jia, S. Tretyakov, and S. Cummer, Highly efficient generation of angular momentum with cylindrical bianisotropic metasurfaces, Phys. Rev. Appl. **11**, 024016 (2019).

[43] J. D. Jackson, *Classical Electrodynamics* (Wiley, New York, 1999), 3rd ed.

[44] A. V. Osipov and S. A. Tretyakov, *Modern Electromagnetic Scattering Theory with Applications* (Wiley, New York, 2017).